



Full length article

## Correlating diameter, mechanical and structural properties of poly(L-lactide) fibres from needleless electrospinning



A. Morel<sup>a,c,1</sup>, S. Domaschke<sup>b,d,1</sup>, V. Urundolil Kumaran<sup>b</sup>, D. Alexeev<sup>c</sup>, A. Sadeghpour<sup>e</sup>, S.N. Ramakrishna<sup>f</sup>, S.J. Ferguson<sup>c</sup>, R.M. Rossi<sup>a</sup>, E. Mazza<sup>b,d</sup>, A.E. Ehret<sup>b,d,\*</sup>, G. Fortunato<sup>a,\*</sup>

<sup>a</sup> Empa, Swiss Federal Laboratories for Materials Science and Technology, Laboratory for Biomimetic Membranes and Textiles, 9014 St. Gallen, Switzerland

<sup>b</sup> Empa, Swiss Federal Laboratories for Materials Science and Technology, Experimental Continuum Mechanics, 8600 Dübendorf, Switzerland

<sup>c</sup> Institute for Biomechanics, Department of Health Sciences and Technology, ETH Zürich, 8093 Zürich, Switzerland

<sup>d</sup> Institute for Mechanical Systems, Department of Mechanical and Process Engineering, ETH Zürich, 8092 Zürich, Switzerland

<sup>e</sup> Empa, Swiss Federal Laboratories for Materials Science and Technology, Center for X-ray Analytics, 8600 Dübendorf, Switzerland

<sup>f</sup> Laboratory for Surface Science and Technology, Department of Materials, ETH Zürich, 8093 Zürich, Switzerland

### ARTICLE INFO

#### Article history:

Received 4 June 2018

Received in revised form 16 August 2018

Accepted 27 September 2018

Available online 29 September 2018

#### Keywords:

Needleless electrospinning

Mechanical properties

Inverse finite element simulations

Boundary conditions

Internal fibre structure

### ABSTRACT

The development and application of nanofibres requires a thorough understanding of the mechanical properties on a single fibre level including respective modelling tools for precise fibre analysis. This work presents a mechanical and morphological study of poly-L-lactide nanofibres developed by needleless electrospinning. Atomic force microscopy (AFM) and micromechanical testing (MMT) were used to characterise the mechanical response of the fibres within a diameter range of 200–1400 nm. Young's moduli  $E$  determined by means of both methods are in sound agreement and show a strong increase for thinner fibres below a critical diameter of 800 nm. Similar increasing trends for yield stress and hardening modulus were measured by MMT. Finite element analyses show that the common practice of modelling three-point bending tests with either double supported or double clamped beams is prone to significant bias in the determined elastic properties, and that the latter is a good approximation only for small diameters. Therefore, an analytical formula based on intermediate boundary conditions is proposed that is valid for the whole tested range of fibre diameters, providing a consistently low error in axial Young's modulus below 10%. The analysis of fibre morphology by differential scanning calorimetry and 2D wide-angle X-ray scattering revealed increasing polymer chains alignment in the amorphous phase and higher crystallinity of fibres for decreasing diameter. The combination of these observations with the mechanical characterisation suggests a linear relationship between Young's modulus and both crystallinity and molecular orientation in the amorphous phase.

#### Statement of significance

Fibrous membranes have rapidly growing use in various applications, each of which comes with specific property requirements. However, the development and production of nanofibre membranes with dedicated mechanical properties is challenging, in particular with techniques suitable for industrial scales such as needleless electrospinning. It is therefore a key step to understand the mechanical and structural characteristics of single nanofibres developed in this process, and to this end, the present work presents changes of internal fibre structure and mechanical properties with diameter, based on dedicated models. Special attention was given to the commonly used models for analyzing Young's modulus of single nanofibers in three-point bending tests, which are shown to be prone to large errors, and an improved robust approach is proposed.

© 2018 Acta Materialia Inc. Published by Elsevier Ltd. This is an open access article under the CC BY-NC-ND license (<http://creativecommons.org/licenses/by-nc-nd/4.0/>).

\* Corresponding authors at: Empa, Swiss Federal Laboratories for Materials Science and Technology, Dübendorf, Switzerland (A.E. Ehret). Empa, Swiss Federal Laboratories for Materials Science and Technology, St. Gallen, Switzerland (G. Fortunato).

E-mail addresses: [alexander.ehret@empa.ch](mailto:alexander.ehret@empa.ch) (A.E. Ehret), [giuseppino.fortunato@empa.ch](mailto:giuseppino.fortunato@empa.ch) (G. Fortunato).

<sup>1</sup> Both authors contributed equally to this work and share first authorship.

## 1. Introduction

Electrospun (e-spun) non-woven membranes are increasingly used in a variety of applications owing to several beneficial properties [1]. The high surface-area-to-volume ratio of the membranes, for example, makes them ideal candidates for applications as drug delivery systems [2–4], catalyst carriers or sensors [1], while the resemblance of the e-spun nano- and microfibre network to e.g. collagen and elastin fibres disposed in the extracellular matrix of soft biological tissues has favoured their use as scaffolds in tissue engineering applications [5–9].

For many of these applications, the mechanical properties at both the nano- and macro-scale play an important role so that their understanding and tailoring represent important steps towards e-spun membranes that are designed to meet selected requirements. Since the network behaviour is largely predefined by the properties of the fibres and their interaction, this poses the essential need for mechanical and structural characterisation of single nano- and microfibres [10].

Single fibre mechanical properties can be determined by three-point bending or tensile set-ups, based on atomic force microscopy (AFM) or specific micromechanical testing (MMT) systems [11]. The axial Young's moduli determined by both methods are generally in sound agreement [12,13] and can be interpreted as a homogenized beam property that averages the fluctuating mechanical properties along and across the fibre as the semi-crystalline structure leads to heterogeneities within the fibres. One advantage of three-point-bending of single e-spun fibres using AFM is the high resolution in displacement and force measurements, which enable accurate assessment of the fibre response to small deflections, typically quantified in terms of the axial Young's modulus [11]. Explained briefly, the fibre spans over a groove of a micro patterned grid while load is applied by the tip of the AFM cantilever. The deflection is recorded and a force-deflection curve is generated. To determine the Young's modulus from these results, both an appropriate theory and boundary conditions have to be assumed. If deflections become larger, tensile stresses due to fibre extension need to be accounted for [11,14–16]. The analytical models commonly used treat fibres over the groove as double-clamped [11,17,18] Euler-Bernoulli beams. Noteworthy, there is a factor of 4 between the forces needed to deflect a double-clamped or double supported slender beam by the same amount.

Unless the fibres are tightly fixed to the AFM grid, e.g., by epoxy glue [19], the fibres are prone to start slipping at a critical deflection [19] thus complicating the use of AFM-based three-point bending tests to investigate the fibre response at large deformations. Micromechanical testing (MMT) devices allow analysing the mechanical properties of single fibres over a wider range of deformations, e.g., in tensile tests [11,20–22], and thus provide access to the non-linear strain regime and material parameters that characterise inelastic behaviour such as yield stress and fibre hardening.

Mechanical tests on single fibres e-spun from various polymers such as polyvinyl alcohol (PVA), polyethylene oxide (PEO), polystyrene (PS) and Nylon-6,6 [18,23–25] revealed that the Young's modulus increases with decreasing fibre diameter, and studies on polycaprolactone (PCL) [21,26,27] and poly(L-lactide) (PLLA) [28–30] fibres showed that the decrease in diameter, mainly controlled by the speed of a rotating drum collector or the spinning solution properties, is also accompanied by an increasing tensile strength [26,27].

These observations of altered fibre mechanical properties can only be explained if the geometric change in fibre cross-section is accompanied by changes of polymer internal structure within the fibres deriving from the formation process, e.g. due to fibre

drawing. Crystallinity has been assessed by differential scanning calorimetry (DSC) [13,30] and wide-angle X-ray diffraction (WAXS) [31], while crystalline orientation is typically investigated by 2D-WAXS on e-spun membranes [32,33] and by side-angle electron diffraction on single fibres [32,34]. Studies demonstrated higher crystalline orientation for thinner fibre diameter of semi-crystalline polymers like PCL and PLLA [27,32]. Furthermore, the properties of the amorphous regions, such as molecular alignment and polymer chain disentanglement, have been studied by polarized Raman spectroscopy [24], DSC [30] and 2D-WAXS [25], showing that the orientation of amorphous polymer chains is higher in fibres of smaller diameters and fibres collected on rotating targets at high take-up velocities, which are undergoing a cold-drawing process during deposition.

Since both crystallinity levels [13,28,30] and intrinsic characteristics of the amorphous phases [24,30] affect the mechanical properties of the polymer and are themselves altered by the fibre formation process (e.g. drawing ratio, environmental conditions) and thus the fibre diameter, the latter indeed becomes an important indicator for the mechanical behaviour of the fibres [23,26,27,29,35]. An abrupt increase in Young's modulus is typically observed for thinner fibres below a critical diameter whose particular value varies depending on the polymer used [25–27].

PLLA belongs to the polyester family. It has been selected in this study for its beneficial properties in contact with living tissues, its industrial relevance, and since it has already been used and studied in electrospinning for biomedical applications [36,37]. The polymer may comprise crystalline and amorphous regions as well as a mesophase, which is defined as an intermediate level of polymer chains order between amorphous and crystalline ordering level, composed of highly aligned amorphous chains e.g. induced by strain [38–41]. A needleless electrospinning device operated on a pilot plant scale and a static collector were used to develop fibres of varying diameters. To the best of the authors' knowledge, no data are available on the mechanical properties of fibres produced by large scale equipment despite their importance towards industrial applications. Furthermore, existing mechanical data on PLLA fibres generated by conventional laboratory electrospinning devices are mainly restricted to Young's modulus, tensile strength and strain at break, while systematic information on the non-linear and inelastic single fibre responses, such as yield stress and hardening, and their dependence on fibre diameter is largely missing. Especially the inelastic properties are important to describe the whole stress-strain curve of a single fibre [28–30] which is essential for predictive simulations of fibrous networks [22,42].

This study aims to probe the elastic, inelastic and morphological properties of needleless e-spun PLLA fibres and the correlation between those factors and to evaluate the consistency between different investigation methods. To this end, single fibres of different diameters were produced by needleless electrospinning and Young's moduli were determined by AFM based three-point bending tests. Thereby, the validity of specific boundary conditions and beam theories were investigated depending on the different fibre diameter. This was studied by means of a finite element (FE) model, used to determine material parameters in a general inverse analysis. Furthermore, an analytic model with a semi-empirical parameter was established. In addition, a MMT device was used to quantify yield stress and plastic hardening in the large strain regime, and their dependence on fibre diameter, in addition to the Young's moduli. Finally, DSC and 2D-WAXS measurements were performed to determine fibres crystalline properties as well as polymer chain alignment in the amorphous phase to establish relationships between those structural characteristics and the measured mechanical properties.

## 2. Materials and methods

### 2.1. Preparation of membranes/single fibres

#### 2.1.1. Materials

PLLA pellets (3100HP Ingeo, Natureworks, USA) were dissolved in dichloromethane (DCM, Macron fine chemicals, Avantor, USA). For the production of single fibres used for mechanical testing, PLLA concentrations of 6% and 8% w/w were used while concentrations ranging from 3.5% to 12% w/w were prepared (Appendix A) for the electrospinning of whole membranes used for structural characterisation methods. To increase the relative permittivity as well as electrical conductivity of the polymer solution, 2–4% w/w dimethylformamide (DMF, VWR chemicals, USA) were added in all solutions, as well as 0.015% w/w tetraethylammonium bromide (TEAB, Sigma Aldrich, USA).

#### 2.1.2. Electrospinning

E-spun fibres were generated using the pilot-plant Nanospider device (NS 1WS500U, Elmarco, Czech Republic) equipped with a spinning carriage module. In this set-up, the solution reservoir continuously moves along a wire source electrode and deposits a thin film of solution on it. Applying a high electrical field forms multiple Taylor cones along the wire, electrospinning jets are pulled toward a counter wire electrode and fibres are deposited onto a paper substrate placed before the counter electrode. Spinning parameters used were: an applied voltage of +20/–17 kV, a reservoir speed of 480 mm/s, a source wire-to-substrate distance of 220 mm, a temperature of 20 °C ( $\pm 1$  °C) and a spinning chamber relative humidity of 20% ( $\pm 3\%$ ). Mean fibre diameter was assessed for each membrane sample ( $n = 100$  fibres) from scanning electron microscopy (SEM) micrographs by analysis with ImageJ software [43]. In order to prepare samples for AFM-based three point bending tests, fibres were directly e-spun onto silicon chips with grooves of 6–7  $\mu\text{m}$  width and 1  $\mu\text{m}$  depth (Sindex, Bioforce Nanosciences, USA) that were glued to the paper substrate before deposition (Fig. 1a). For MMT, fibres were prepared by collecting fibres during several seconds on a rectangular cardboard frame (50 mm  $\times$  150 mm) fixed to the paper substrate. The fibres were then transferred on dedicated clamps (see Section 2.4.1).

### 2.2. Scanning electron microscopy

Prior to imaging, samples were sputter-coated with a 7 nm-thick gold palladium layer (Leica EM ACE600, Leica Microsystems, Germany). SEM (Hitachi s-4800, Hitachi High-Technologies Corporation, Japan) was performed using an acceleration voltage of 2 kV and 10 mA current flow.

### 2.3. AFM-based three-point bending tests

#### 2.3.1. Experimental procedure

The three-point bending tests were performed with an AFM (MFP-3D, Asylum Research, USA) using cantilevers (OMCL-AC160TS-R3, Olympus, Japan) with a tetrahedral tip with a radius of 7 nm (from the manufacturer details) and spring constants ranging from 14 to 25 N/m, calibrated by thermal noise method [44]. After mounting the sample on the AFM stage, fibres oriented perpendicularly across a groove of the silicon chip were located with the camera of the AFM and the specific location was then captured by AC mode imaging (Fig. 1b). The acquired 3D-image of the fibre geometry was used to ensure that the fibre was straight over the groove without crimp or slack. Afterwards, the imaging mode was switched to contact mode. The fibre was then bent by pushing the cantilever tip onto it at the centre of the groove, determined from the AFM image (Fig. 1b), at a speed of 2  $\mu\text{m/s}$  by using pick point option in the MFP3D software. The fibres were deflected and the force  $F$  and central displacement  $w_B$  were recorded. In order to correct for the indentation  $w_A$  of the tip into the fibre, force-displacement curves were also recorded for fibres portions lying on the hard silicon substrate and the effective deflection  $\hat{w}(F) = w_B(F) - w_A(F)$  was calculated. Finally, fibre diameters  $D$  and the exact groove widths, corresponding to the free-spanning length  $L$  of the fibre were assessed from SEM (Fig. 1a) using ImageJ software.

#### 2.3.2. Analytical Timoshenko beam model

Euler-Bernoulli beam theory is usually used to analyse AFM-based three-point bending tests when the central deflection  $\hat{w} = w(z = L/2)$  is small compared to the fibre diameter  $D$ , typically  $\hat{w} < D/2$  [11,16]. In this case, the relation between force  $F$  and  $\hat{w}$  of the fibre reads  $\hat{w} = (FL^3)/(cEI)$  with  $I = \pi D^4/64$  the second moment of inertia for circular cross-sections,  $E$  the Young's modulus and  $c$  a parameter depending on the assumed boundary conditions i.e. the clamping method. The latter takes values of either  $c = 192$  for double-clamped (DC, Fig. 2a) or  $c = 48$  for double supported (DS, Fig. 2b) beams.

The typically only moderate ratios between groove width, resp. free fibre length, and fibre diameter call for caution when employing the Euler-Bernoulli beam theory that applies to slender beams. As shear deformations become increasingly relevant as  $L/D < 10$  [45], Timoshenko beam theory was used in this work, leading to an additional deflection term  $(FL)/(4GA\eta)$  [46], where the shear modulus  $G = E/[2(1 + \nu)]$  of a linear elastic isotropic material was assumed,  $\nu$  denotes Poisson's ratio,  $A = \pi D^2/4$  is the cross-sectional area and  $\eta = 0.9$  the shear correction factor for circular cross-sections [47].

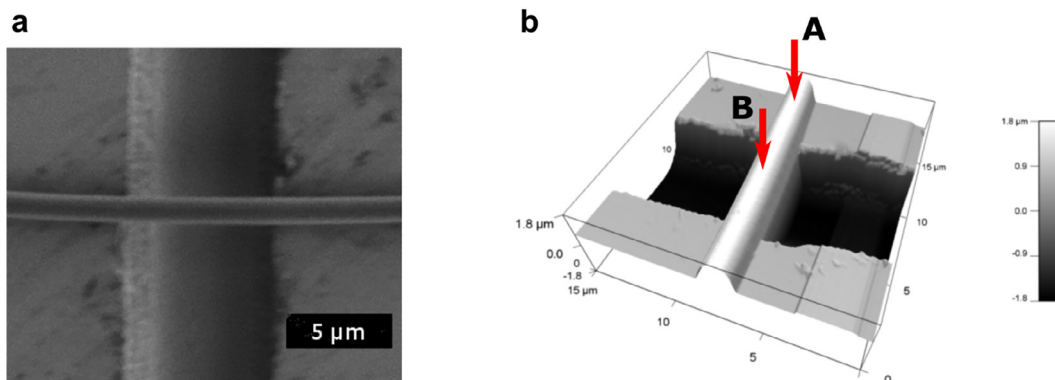


**Fig. 1.** Single fibre deposition. (a) SEM of a fibre lying over a groove of the silicon chip. (b) AFM AC mode imaging. AFM force-displacement measurements onto the fibre are conducted on the substrate (point A) and over the groove (point B).

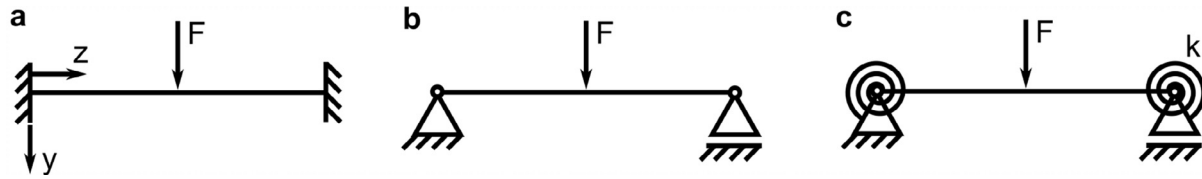


**Fig. 2.** Model of the three-point bending test. (a) Double clamped (DC) boundary conditions (b) double supported (DS) boundary conditions and (c) torsional springs at the boundaries (TS).

Finally, since it is assumed that the fibre sticks to the substrate only at its bottom contact area (validated by AFM measurements, see Section 3.2), while the remaining fibre surface is unconstrained, the fibre may experience shear in the  $x, z$  plane (Figs. 2a and E.1) different from a double-clamped beam. To this end, the resistance to rotation at the boundary was modelled by a torsional spring with spring constant  $k$  (Fig. 2c) that connects the rotational moment  $M$  at the beam ends to the rotation  $\varphi$  of the cross-section of the Timoshenko beam by  $M = k\varphi(z = 0)$ . With  $I = \pi D^4/64$ ,  $\hat{w} = w|_{z=L/2}$  and the boundary conditions  $w(z = 0) = 0$ ,  $\varphi(z = L/2) = 0$ ,  $El \frac{d^2\varphi}{dz^2}|_{z=0} = -\frac{F}{2}$ , this leads to

$$\hat{w} = \frac{FL^3}{48EI} \kappa + \frac{FL}{4GA\eta}, \quad (1a)$$

$$\kappa = \left(1 - \frac{3L}{8\left(\frac{EI}{k} + \frac{l}{2}\right)}\right). \quad (1b)$$

A purely mathematical limit analysis of Eq. (1b) reveals that  $\kappa \rightarrow 1/4$  for  $k \rightarrow \infty$  and  $\kappa \rightarrow 1$  for  $k \rightarrow 0$ .  $\kappa = 1/4$  leads to the DC solution, while  $\kappa = 1$  leads to the DS solution. This agrees with the physical stand point as  $k \rightarrow \infty$  reflects the infinite resistance to rotation provided by a clamp (Fig. 2a), and  $k \rightarrow 0$  reflects free rotation, as possible on a simple support (Fig. 2b).

### 2.3.3. Inverse finite element (iFEM) analysis

A three-dimensional FE-Model of the three-point bending test was used to compute the force-displacement curves for given material parameters (Abaqus/Standard 2016, Dassault Systèmes Simulia Corp., Johnston, RI, USA). One quarter of the set-up was modelled using symmetry boundary conditions (Fig. 3). The model was meshed with quadratic brick elements (C3D20) with an average element edge length of 10% of the fibre diameter and a locally refined mesh at the transition to the substrate. The substrate was modelled as an analytic rigid surface, and initial contact points of the fibre with the substrate were fixed whereas penetration was prevented by hard frictionless contact. Isotropic linear elastic material properties were used, with Poisson's ratio  $\nu = 0.4$  [48].

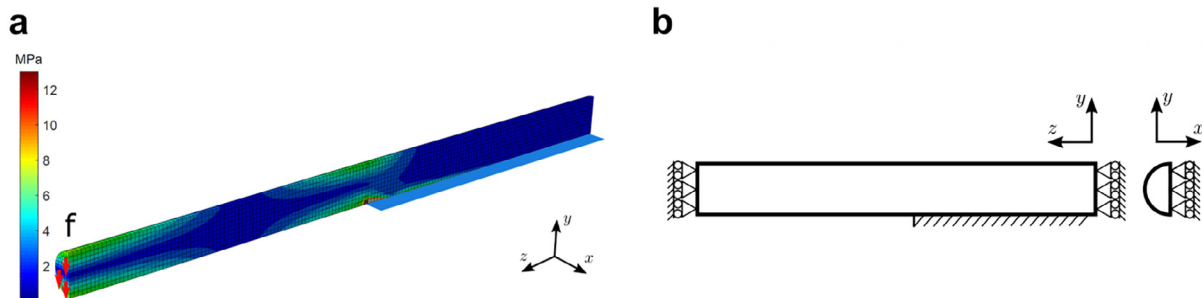


**Fig. 3.** 3D-numerical model. (a) Finite element model of the fibre over the groove. A distributed force  $f$  at the front face leads to a deformation. The maximal von Mises stress for the plotted range was set to 13 MPa to show the stress distribution apart from the concentration at the transition to the substrate. Due to symmetry only a quarter of the fibre was modelled. (b) Boundary and symmetry conditions of the numerical model.

The force  $F$  modelled as a surface traction was distributed over the central cross-section and the corresponding displacement  $\hat{w}_{FE}$  at the centre was determined. For each experimental force-displacement curve, the Young's modulus  $E$  was identified by an inverse optimisation loop reducing the quadratic error of the displacement in the center  $\Omega = \sum_i (\hat{w}_i - \hat{w}_{FE}(F_i))^2$ , on  $i = 1, 2, \dots, n$  data points of the force deflection curve, controlled by a MATLAB (R2016b, The MathWorks Inc., Natick, MA, USA) routine. The value of  $E$  thus found was inserted in Eq. (1) and  $k$  was calculated so that the equation was satisfied.

## 2.4. Micromechanical testing

### 2.4.1. Experimental procedure

The FT-MTA02 Micromechanical Testing and Assembly Station equipped with a FT-S1000 Microforcing Sensor Probe force sensor (FemtoTools AG, Buchs, Switzerland) was used to conduct combined bending-tensile tests. To clamp the fibres for testing, dedicated clamps consisting of three metal plates with oblong parallel holes with dimensions of 13 mm  $\times$  3 mm were used (Fig. 4). After positioning the fibre across the thin middle plate perpendicular to the oblong holes (Fig. 4a) the system was clamped by the two thicker plates (Fig. 4b) and fastened by screws. The part of the fibre passing the central slit was used for SEM to determine the fibre diameter, whereas the part passing one of the outer slots was used for a three-point bending-tension test (Fig. 4b). To manipulate the fibre, a tungsten hook (FWT-2-120-hook, Pacific Instruments) was attached to the force sensor using a UV curing glue (Loctite AA 3494). The microrobotic system was used to grab and pull the fibre at half its free length (Fig. 4c). The digital microscope of the MMT was used to monitor the fibre position, which was found to be straight between the two clamped ends without crimp or slack due to the sample preparation. The displacement  $w_{hook}$  of the hook as well as the corresponding force were recorded by the system.

### 2.4.2. Extraction of mechanical properties of micromechanical testing

The MMT system allows for large deflections such that the response turns from a bending-dominated initial phase over to a

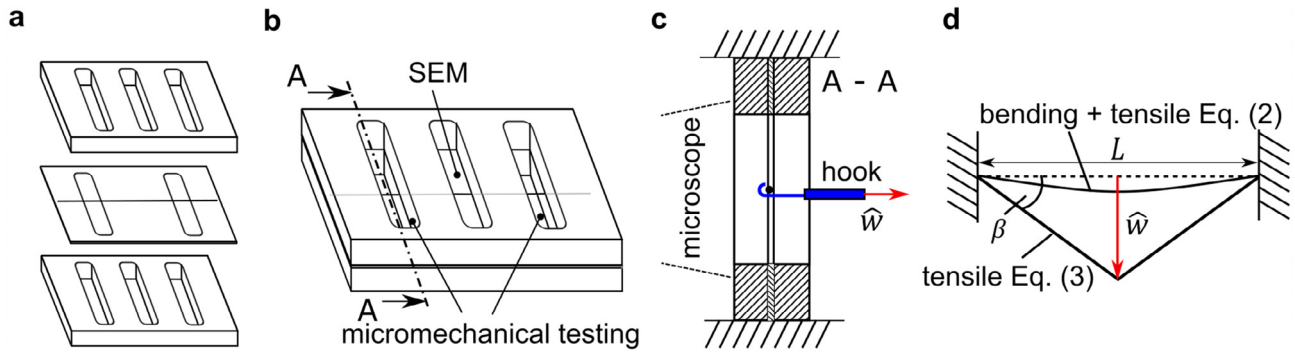


**Fig. 4.** MMT testing procedure. (a) Clamping system with the fibre lying on the middle plate. (b) Fibre clamped between the outer plates. (c) Sketch of testing set-up with hook pulling on the fibre. (d) Different loading stages of a double clamped beam in a three-point bending arrangement. Note that scales of the sketch do not match the scales of the experiment.

mixed bending- and tension response to a purely tension-dominated behaviour (Fig. 4d). Since the tested fibre segments with length  $L = 3$  mm have a ratio  $L/D > 1000$  the Euler-Bernoulli beam theory applies, and an amendment to account for the tensile stresses was proposed by Heidelberg et al., providing the force  $F$  for a given displacement  $\hat{w}$  as [11,16]

$$F = \frac{192EI}{L^3} f(\gamma) \hat{w}, \quad (2a)$$

$$f(\gamma) = \frac{\gamma}{48 - \frac{192 \tanh^2 \frac{\gamma}{4}}{\sqrt{\gamma}}}, \quad (2b)$$

$$\gamma = \frac{6\epsilon(140 + \epsilon)}{350 + 3\epsilon}, \quad (2c)$$

$$\epsilon = \hat{w}^2 \frac{A}{I}. \quad (2d)$$

Due to the lower force resolution of the MMT ( $\sim \mu\text{N}$ ) compared to AFM ( $\sim \text{nN}$ ) the linear, bending dominated response of the experimental force-deflection curve is strongly affected by measurement noise. Moreover, the noise complicates identifying the zero-position from the force response, i.e. the displacement  $w_{\text{off}}$  at which the hook first comes into contact with the fibre when moving from its initial position at the beginning of the experiment. Therefore, an offset  $w_{\text{off}}$  was introduced and subtracted from the total displacement  $w_{\text{hook}}$ , so that  $\hat{w} = w_{\text{hook}} - w_{\text{off}}$ , and both  $E$  and  $w_{\text{off}}$  were determined by fitting the force-deflection curves to Eq. (2). For the fitting only the data in the small elastic range between  $\hat{w} = 0$  and the initiation of yielding was used, in which Eq. (2) is valid. In the purely tensile-dominated phase, engineering strain  $\epsilon$  and stress  $P$  in the two “halves” of the fibre were calculated by trigonometry

$$\epsilon(\hat{w}) = \frac{2 \left( \sqrt{\hat{w}^2 + \left(\frac{L}{2}\right)^2} - \frac{L}{2} \right)}{L}, \quad (3a)$$

$$P(\hat{w}) = \frac{F}{2 \sin(\beta(\hat{w}))A}, \quad (3b)$$

$$\beta(\hat{w}) = \tan^{-1}(2\hat{w}/L). \quad (3c)$$

The stress-strain plots were approximated by a bi-linear representation with a first linear function of slope  $E$  to describe the elastic region, and another one with slope  $H$  to characterise the hardening, i.e. the further increase of stress with strain in the plastic regime. While  $E$  was predefined by analysis of the data with Eq. (2),  $H$  was

determined by linear regression. The yield stress  $P_Y$  was defined by the intersection of the two lines. Noteworthy,  $P$  and  $P_Y$  are nominal stresses and differ from the Cauchy-stresses at finite strain.

## 2.5. Fibre internal structure characterisation

### 2.5.1. Differential scanning calorimetry

Samples of 5–7 mg were inserted into aluminium crucibles and closed with lids and introduced into the DSC (214 Polyma, NETZSCH, Germany). Temperature was increased from 25 °C to 220 °C at a heating rate of 10 °C/min. Resulting plots were analysed with NETZSCH Proteus software. Crystallinity  $\bar{\chi}$  was calculated from the melting enthalpy  $\Delta H_m$ , the cold crystallization enthalpy  $\Delta H_c$  and the melting enthalpy of pure crystalline PLLA  $\Delta H_o$  (93.7 J g<sup>-1</sup>) [49]

$$\bar{\chi} = \frac{\Delta H_m - \Delta H_c}{\Delta H_o}. \quad (4)$$

### 2.5.2. 2D-SAXS and 2D-WAXS measurements

E-spun membranes were used for SAXS and WAXS measurements. The experiments were carried out with the Nanostar instrument (Bruker AXS GmbH, USA) equipped with a VANTEC-2000 detector. Cu K- $\alpha$  radiation with a wavelength  $\lambda$  of 0.154 nm was used as incident beam generated by the X-ray source (Incoatec GmbH, Germany). Scattered photons were collected during 60 min for each sample. Sample-detector distances were 107 cm for SAXS and 12 cm for WAXS measurements.

To investigate the orientation distribution of the molecular chains in the amorphous phase within the fibres, membrane samples were drawn with an in-situ tensile stage in order to get high alignment of the fibres [33,50]. For this purpose, samples were cut into rectangular shapes of 6 mm  $\times$  25 mm and were clamped on the stage before being drawn at defined strain (5%, 10%, 20%, 30%, 40%, and 50%). Fibre alignment with strain was assessed by in-situ SAXS tensile testing using Ruland’s method [33,51,52] (Appendix B) for membranes e-spun from 6% and 10% w/w PLLA solutions (see fibre diameters Table 1). This method assumes the presence of air microvoids oriented in the fibre axis generated by drawing forces during the electrospinning process [33,41,53]. As the difference of electron density between the air and the polymer is high, the scattering from microvoids results in a streak signal near to the beam stop [52] (Fig. 9d). Proper analysis of the streak patterns using Ruland’s method enables the evaluation of the microvoids misorientation, and thus of the fibres misorientation within the membrane [33,51] (Appendix B). Considering the orientation distribution of the fibres as a Lorentz function centred on the membrane stretching direction, the obtained misorientation value

corresponds to the width of this function. A value of  $0^\circ$  would describe fully aligned fibres in the strain direction.

WAXS measurements were performed on membranes produced from solution of 6%, 8% and 10% w/w PLLA. In order to obtain samples with similar fibre alignment, results from above SAXS measurements were used to determine respective elongation strain to which membranes with different fibre diameter were drawn. 1D-WAXS azimuthal profiles (Appendix C, Fig. C.1b) were obtained by integrating the intensity between diffraction angles ( $2\theta$ )  $10$ – $19^\circ$ . The morphological anisotropy in the fibre structure was first described by the fraction of oriented polymer chains  $F_{or}$  within the fibres. This parameter was calculated by Eq. (5) with  $A_{or}$  defined as the area under of the azimuthal profile but above the baseline, and  $A_b$  as the area below the baseline corresponding to randomly oriented polymer chains [54]

$$F_{or} = \frac{A_{or}}{A_{or} + A_b} \quad (5)$$

Secondly, the area  $A_{or}$  corresponding to oriented chains was further characterised by peak fitting with the software Origin 2017 in order to distinguish the contribution of the different phases (amorphous, crystalline and mesophase) (Appendix C). For this purpose a Gaussian function was fitted on the azimuthal profiles for each phase and their respective orientation factors  $f_H$  were defined based on the Herman's orientation function [55]

$$f_H = \frac{3\langle \cos^2(\Phi) \rangle - 1}{2} \quad (6)$$

where  $\Phi$  corresponds to the angle between the fibre axis and the polymer chain axis. In this study, the simplified calculation of the orientation function (Eq. (7)) was used [33,56] with FWHM corresponds to the full-width-at-half-maximum of the corresponding Gaussian function.

$$f_H = \frac{180^\circ - FWHM}{180^\circ} \quad (7)$$

An orientation factor of 0 would correspond to an isotropic arrangement of the polymer chains. Increasing value goes along with narrower orientation distribution and a maximal value of 1 characterises polymer chains fully oriented in the same axis.

## 2.6. Error estimation of mechanical testing

To estimate the errors in the determined material parameters, i.e.  $E$  in AFM and  $E$ ,  $P_Y$  and  $H$  in MMT, a propagation of error anal-

ysis was performed. Using the accuracies of the measurement instruments and subsequent analysis, and the analytic solutions (Eqs. (1) and (2)), error estimates of  $\sim 23\%$  for AFM based testing and  $\sim 29\%$  for MMT were determined (Appendix D).

## 3. Results

### 3.1. Electrospinning

DCM is very volatile, non-conductive, and, given its lower toxicity, it was preferred as main solvent over chloroform, which had been used in preliminary studies. By controlling the polymer concentration from 3.5% to 12% w/w, membranes with mean fibre diameters ranging from 200 to 1100 nm (with a diameter distribution of  $\pm 40\%$  within a sample) were produced (Fig. 5). For single fibre mechanical testing, polymer concentrations of 6% and 8% were chosen to produce single fibres with diameters between 200 and 1400 nm. Homogenous fibre formation was obtained by adding 2–4% DMF, depending on polymer concentration, and salt (TEAB) to increase the electrical conductivity (see Appendix A, Table A.1).

### 3.2. AFM-based three-point bending tests and analysis

PLLA fibres with different diameters were tested by three-point-bending using AFM. Force-deflection curves of the fibre on the substrate and on the groove were recorded (Fig. 6a), and fibre diameter  $D$  as well as groove width  $L$  were determined for each sample. A repeated test with the same fibre and imaging of the fibre after the test by SEM confirmed that the fibre did not slip and firmly adhered to the substrate. Young's moduli  $E$  of tested fibres were determined by iFEM analysis and revealed a dependence of  $E$  on fibre diameter, well captured by a power law (Fig. 6b). Error bars indicate the estimates through propagation of errors analysis (Appendix D). Furthermore, the measurements indicate that for fibre diameters larger than around 800 nm  $E$  is almost constant whereas  $E$  can increase by up to a factor of 10 for very thin fibres compared to the thick ones.

Fitting the theoretical approach (Eq. (1)) to the experimental data with the previously determined  $E$  from the iFEM analyses revealed a clear dependence of the spring constant  $k$ , and thus the factor  $\kappa$ , on the fibre diameter (Fig. 7a, green squares). Neither double clamped ( $\kappa = 1/4$ ) nor double supported ( $\kappa = 1$ ) conditions represent the set-up adequately, and the bottom-fixed fibre behaves somewhere in between these cases.

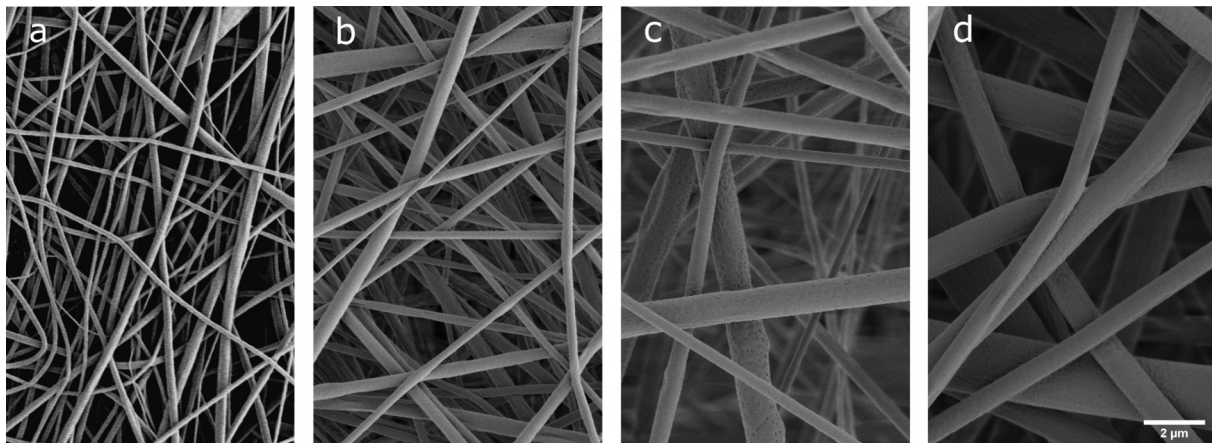
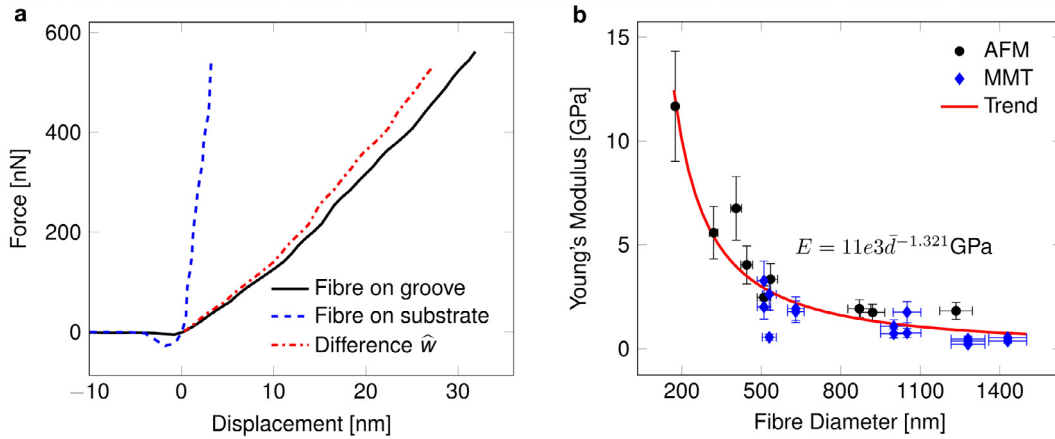
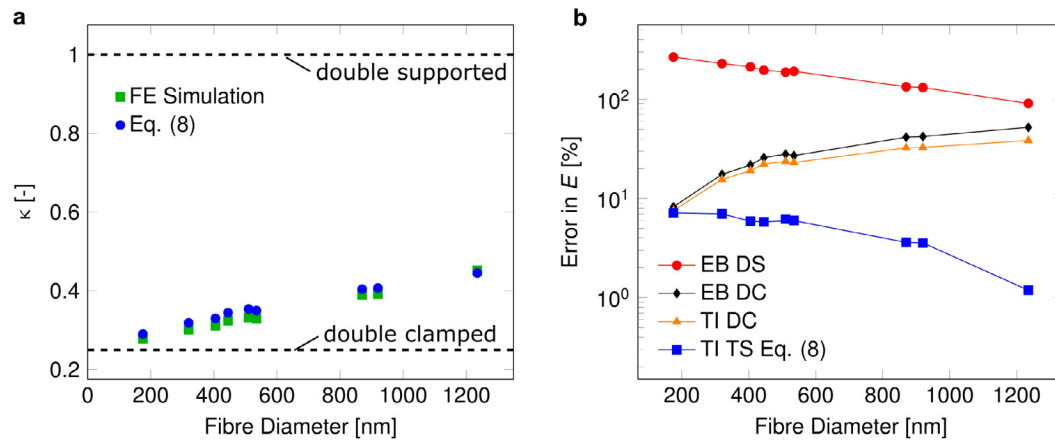


Fig. 5. SEM images of electrospun membranes: developed from solutions with PLLA concentration of (a) 3.5%, (b) 6%, (c) 8%, (d) 12% w/w. Respective mean fibre diameters are  $200 \pm 70$  nm,  $390 \pm 150$  nm,  $630 \pm 290$  nm, and  $1100 \pm 420$  nm.



**Fig. 6.** AFM-based and MMT measurements. (a) Force-displacement curves by AFM-based three-point bending experiments. (b) Young's modulus vs fibre diameter for AFM-based and MMT measurements. Power law fit where  $\bar{d} = D/(1\mu\text{m})$ ,  $R^2 = 0.88$ ). Error bars indicate the estimates from the propagation of errors analysis (Appendix D).



**Fig. 7.** Three-point bending: influence of boundary conditions. (a) Dependence of the boundary factor on the fibre diameter evaluated by FE simulations and by analytic expression (Eq. (8)). (b) Error in the evaluation of the Young's modulus compared to the FE simulations by Euler-Bernoulli theory with DC (EB DC) and DS (EB DS) boundaries, by Timoshenko theory with DC boundaries (TI DC) and by calculating the boundary factor analytically (TI TS) by expression (Eq. (8)).

Moreover, the semi-empiric formula  $k = EI/\alpha D$  derived in Appendix E with the simplification  $\alpha = 1$  allows approximating the factor  $\kappa$  that scales between the boundary conditions as

$$\kappa \approx \left(1 - \frac{3L}{8(D + \frac{L}{2})}\right). \quad (8)$$

Comparing this result (blue dots in Fig. 7a) to the values determined by iFEM (green squares) shows sound agreement ( $R^2 = 0.89$ ) and suggest Eq. (8) as an excellent approximation. The errors in  $E$  compared to the iFEM results, i.e.  $|E_{\text{ana}} - E_{\text{iFEM}}|/E_{\text{iFEM}}$ , were evaluated for different analytical approaches (Fig. 7b): Euler-Bernoulli (EB) theory with DS and DC boundaries, Timoshenko (Ti) theory with DC boundaries, and Timoshenko theory with torsional springs (TS), with  $\kappa$  determined by Eq. (8). Fig. 7b reveals a major error obtained with DS boundary conditions. Also DC boundaries lead to substantial errors >50% for large diameters, whereas the error strongly reduces for thinner fibres. The comparison between Euler-Bernoulli (EB DC) and Timoshenko (Ti DC) theories (Fig. 7b) also reveals the influence of the shear contribution in the evaluation of  $E$ . Only the analytical theory with springs at the boundaries (Eqs. (1a) and (8)) leads to errors consistently below 10% (Fig. 7b)

for all tested diameters, and devoid of a trend to increase with  $D$ . The observed decreasing error with  $D$  suggests that the empiric relation between  $k$  and  $D$  with  $\alpha = 1$  (Appendix B) is a better approximation for thicker fibres.

### 3.3. Micromechanical testing

During micromechanical testing fibres were loaded until failure occurred, a typical force-displacement curve is shown in Fig. 8a, and the corresponding stress-strain curve based on Eq. (3) is shown in Fig. 8b together with the bi-linear fit. Note that the deviations close to the origin are a result of an invalid interpretation of the data by Eq. (3) in the initial, bending dominated regime. The Young's modulus  $E$  determined for a range of different fibre diameter is shown in Fig. 6b (blue diamonds) together with the AFM measurements.

Similar to  $E$ , yield stress  $P_y$  and hardening  $H$  determined for a range of different fibre diameters likewise show a clear trend to increase for lower fibre diameters (Fig. 8c, d). The sensitivity to diameter becomes small for thicker fibres  $D > 1200$  nm, and both  $P_y$  and  $H$  increase by approximately one order of magnitude when  $D$  is halved.

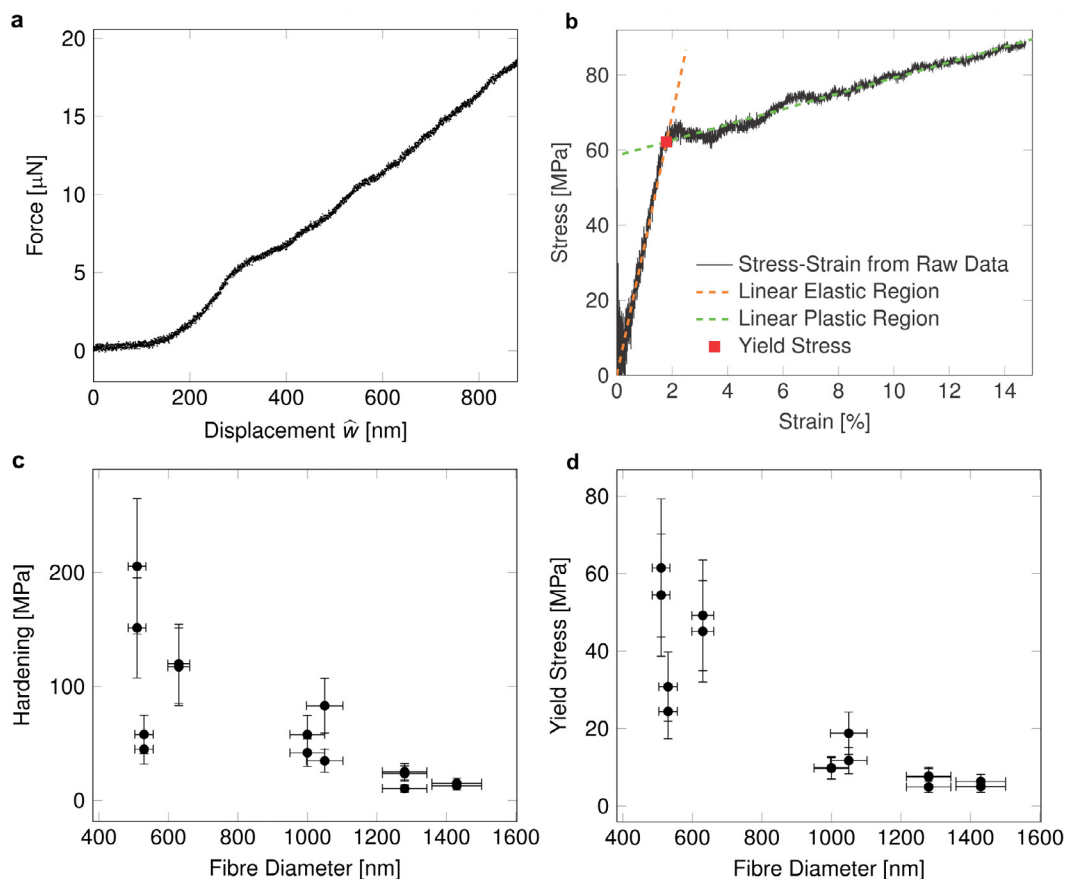


**Fig. 8.** MMT data extraction. (a) Force-displacement curve of single fibre testing by MMT. (b) Converted force-displacement to stress-strain curve by Eq. (2). (c) Hardening and (d) yield stress of single fibres in dependence of the fibre diameter revealed by MMT. Error bars indicate the estimates from the propagation of errors analysis.

### 3.4. Fibre internal structure

Crystallinity level and molecular orientation of the amorphous phase on whole membrane samples were first assessed from DSC thermograms showing typically three transition points corresponding to the glass transition temperature, the cold crystallization and the melting peak (Fig. 9a) [57]. The crystallinity level shows a clearly decreasing dependence on the fibre diameter (Fig. 9b) especially for lower diameters. For membranes incorporating fibre diameters above 800 nm the crystallinity remains at almost constant values as found for the dependency of  $E$ .

The cold crystallization (CC) exothermic peak corresponds to a molecular rearrangement during which oriented amorphous chains turn into crystalline structures. Higher level of chain orientation in the amorphous phase favours CC at lower energy and thus, at lower temperature [30]. A gradual reduction of CC peak temperature was observed with decreasing mean fibre diameter of e-spun PLLA membranes (Fig. 9a and c).

The equatorial (=vertical) SAXS streak patterns are generated by the diffraction from air voids inside the fibres and elongated in its axis direction [33,51]. This signal was used to measure fibres misorientation within the membrane as a function of strain (Appendix B). From obtained curves (Fig. 9e), one can notice that smaller fibres (6% PLLA, see fibre diameter in Table 1) tend to align with lower misorientation width at same strain value compared to thicker fibres (10% PLLA).

For the evaluation of the fibre structural anisotropy by WAXS, strains were individually selected from the misorientation-strain

curves (Fig. 9e) for the different samples in order to get similar fibre alignment. 30% strain was chosen for membranes from 6% PLLA, 40% for membranes from 10% PLLA and an intermediate value of 35% strain for membranes from 8% PLLA. WAXS profiles of PLLA membranes revealed a broad diffraction peak (Fig. 9f) corresponding to material regions with non-constant distance between polymer chains and, thus, characteristic for non-crystalline phases. Only the membrane from 6% PLLA shows a small peak at  $2\theta = 16.5^\circ$  corresponding to the co-existence of crystalline and meso-phase [40]. This peak position is characteristic for the (2 0 0/1 1 0) crystal planes [58] of PLLA. Mesophase was also revealed in the other samples of higher fibre diameter after careful peaks analysis (Appendix C) and on DSC measurements as an endothermic ( $T_{\text{end}} = 68^\circ\text{C}$ ) peak in the late stage of the glass transition (Fig. 9a, black star) [39]. The peak is translated as the melting of the mesophase which is only stable below the glass transition temperature.

The fraction of oriented polymer chains  $F_{\text{or}}$  within fibres was calculated from azimuthal profiles. Table 1 shows that  $F_{\text{or}}$  increases for thinner fibres. Furthermore, peak fitting enabled the distinction of the contributions of the amorphous phase and the mesophase in the azimuthal profile (Appendix C) and, thus, the evaluation of corresponding orientation factors. Similar to the cold crystallization peak extracted from DSC curves, these results from WAXS experiments show a narrower chain orientation distribution in the amorphous phase  $f_{\text{H, amorphous}}$  in networks of decreasing fibres sizes (Table 1). Mesophase was highly oriented along fibre axis in all samples, independently of the fibre diameter ( $f_{\text{H, mesophase}} = 0.90 \pm 0.01$ ).

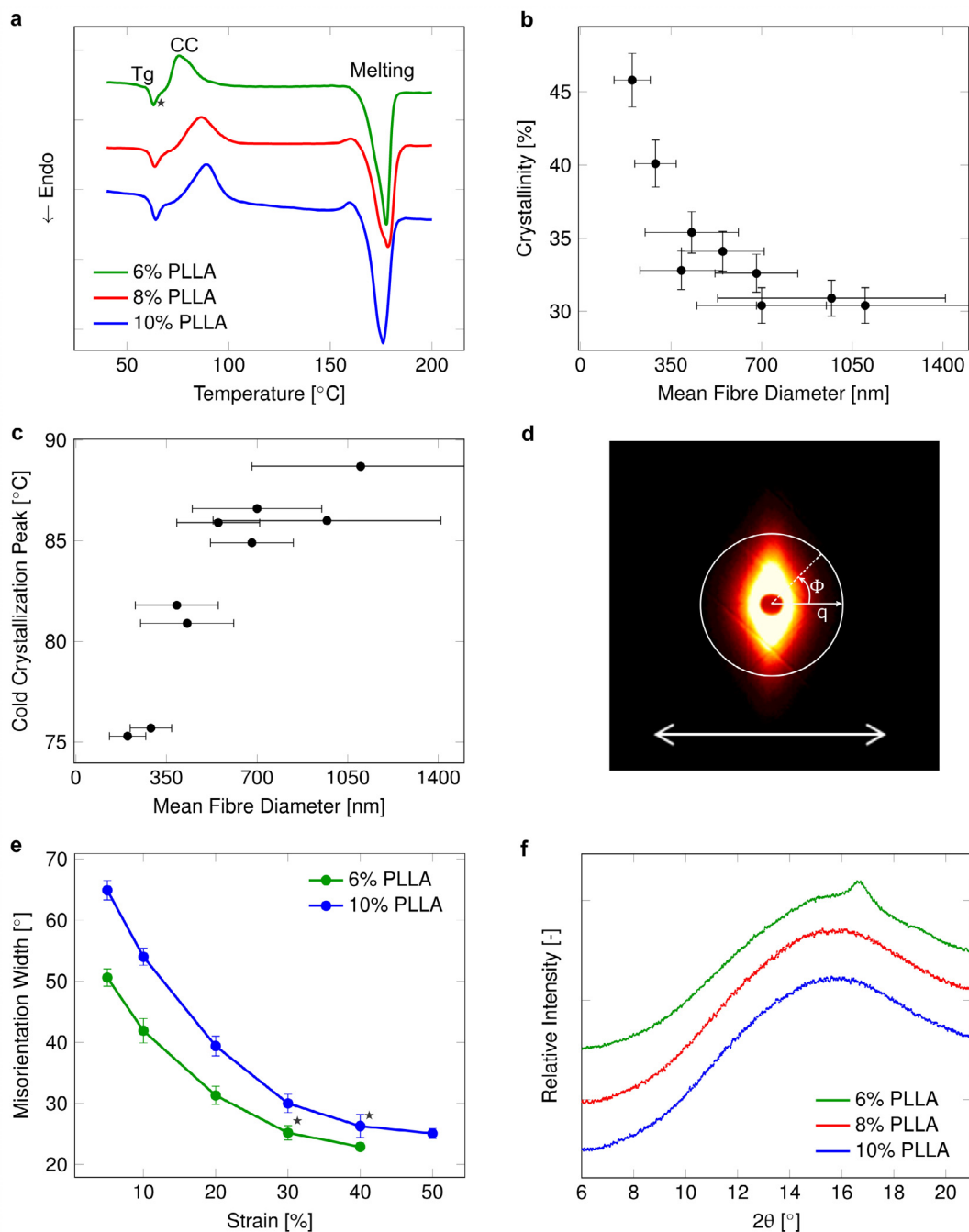


**Fig. 9.** Fibre structure characterization. (a) DSC measurements showing glass transition (Tg), cold crystallization (CC) and melting. The arrow shows the direction of endothermic events (Black star: endothermic peak characteristic for the mesophase melting). (b) Crystallinity level (4% error for enthalpies calculation) and (c) cold crystallization temperature of membranes in function of the mean fibre diameter (SD of  $n = 100$  fibres within tested membranes) (d) 2D-SAXS of membranes prepared from 10% PLLA and drawn to 40%. The pattern is elongated in the equatorial (=vertical) axis due to the streak signals. The bottom arrow shows the elongation direction, thus the fibre orientation in the real space. Radial  $q$ -axis and azimuthal  $\phi$ -axis are represented. (e) Evolution of the misorientation width (Error bars: deviation between values obtained from the two SAXS pattern hemispheres) in function of elongation strain. Black stars show respective elongation strain used for WAXS measurements. (f) 360°-azimuth integrated WAXS profiles.

**Table 1**

2D-WAXS analysis. Influence of the fibre diameters (SD of  $n = 100$  fibres within tested membranes) tailored by PLLA concentration of the electrospinning solutions on the fraction of oriented polymer chains  $F_{or}$  and the corresponding orientation factor of the amorphous phase  $f_{H, amorphous}$  (SD of  $n = 2$  locations measured).

[PLLA] [w/w]	Fibre $\emptyset$ [nm]	$F_{or}$	$f_{H, amorphous}$
10%	$890 \pm 365$	0.10	$0.51 \pm 0.01$
8%	$630 \pm 290$	0.12	$0.53 \pm 0.01$
6%	$390 \pm 145$	0.16	$0.56 \pm 0.01$

#### 4. Discussion

Needleless electrospinning offers the possibility to produce large scale membranes composed of submicron-sized fibres [59,60]. The use of a pilot scale device for the generation of structures composed of PLLA fibres has been barely reported yet. In classic needle based electrospinning, 10–20% of non-solvents or poor solvents, such as DMF or DMSO, are added to increase the dielectric constant of the solution [31]. This is an important parameter to

obtain homogenous fibres and high throughput as more charges are incorporated within the jet leading to, e.g., a higher drawing ratio during fibre formation. However, when used with the needleless device, the polymer solution is for a short time in contact with air after being deposited on a source electrode wire, before an electrospinning jet is formed. In such conditions, DCM evaporated rapidly and DMF remainders formed a solidified gel with PLLA on the wire. Macroscopic droplets were ejected on the substrate and after a few minutes the electrospinning process was completely blocked. This issue was solved by reducing DMF ratio, thus adding DCM to hinder gel formation, and adding TEAB to compensate for the reduced conductivity. In that way, homogenous continuous fibre formation was achieved until the polymer solution reservoir emptied.

Single fibre Young's modulus evaluated by AFM-based three-point bending and MMT in dependence on fibre diameter are in agreement with previous studies, in which Young's moduli between 0.4 and 1.25 GPa were measured for PLLA fibres with diameter above 800 nm, while below 800 nm, values increased for thinner fibres ( $\sim 7$  GPa for a diameter of  $\sim 150$  nm) [13,28,29]. Hence, polymer fibres generated by the needleless electrospinning procedure show similar mechanical properties as those obtained by needle-based systems. In order to analyse the experimental AFM data, an iFEM approach was developed in which the fibre was attached to the substrate only at its bottom contact line (Fig. 3) to reflect the situation in the experiment. This detailed model is assumed to provide reliable estimates of Young's modulus, which were therefore compared with the classical analytical beam models using DC or DS boundary conditions. The comparison showed the large impact of the chosen boundary conditions and indicated large errors for both of them (Fig. 7). A convergence to DC boundaries for lower diameters and a trend towards DS boundaries was observed for larger diameters (Fig. 7), which is in line with experimental results on silver nanowires [61]. Therefore, an alternative representation was proposed, modelling the fibre as a Timoshenko beam supported by torsional springs (Fig. 2c). Despite its simple form, the resulting analytic and semi-empiric formula (Eq. (1a) with Eq. (8)) provides a consistently low error for the determined Young's modulus over the whole range of tested fibre diameters, in contrast to classical theories with DC and DS boundary conditions.

Instead of using a change of the force-displacement curve as an indicator of the reference state of the fibre in MMT measurement, Eq. (2) was fitted to the experimental data, treating the offset displacement  $w_{off}$  as a fitting parameter. The reference state is thus determined by a numerical, reproducible algorithm and does not depend on a subjectively chosen force threshold. The Young's mod-

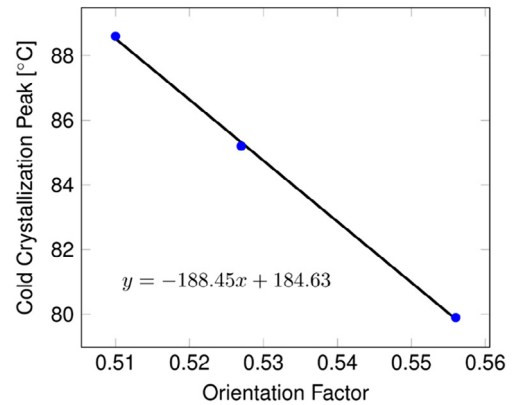


Fig. 11. Linear relationship between amorphous orientation factors measured by WAXS and corresponding cold crystallization temperature from DSC.

ulus  $E$  determined by MMT (blue diamond in Fig. 6b) is in sound agreement with the AFM measurements, despite the simplifying assumption of isotropy used for their analysis through iFEM and the Timoshenko beam model. This suggests that the two measuring techniques and corresponding methods for data interpretation can be used complementarily [12,13] to determine effective axial fibre properties. One power law fit  $E = 11e3d^{-1.321}$  GPa (Fig. 6b) was used to capture the trend of both data sets obtained by AFM and MMT testing. While the change of Young's modulus, and also failure stress and strain have been reported for PLLA fibres before [13,28–30], we here provide the diameter dependent yield stress  $P_y$  and hardening  $H$ , which allow reconstructing a bi-linear representation of the stress-strain curve (Fig. 8b). Failure strains, on the other hand, are not reported since failure of the fibre in the MMT set-up is prone to occur due to high localized loads at the hooking or clamping sites, and are therefore not representative of the material. As a further limitation of the current set-up, it is difficult to assess fibres with diameters below 500 nm due to resolution limitations of the optical camera and difficulties in handling. Therefore, no data of hardening and yield stress values for fibres below 500 nm could be measured.

In order to understand the evolution of the mechanical properties with fibre diameter, fibre internal structure was investigated. DSC measurements revealed an increase of crystallinity and of molecular orientation within the amorphous phase, shown as a reduced CC temperature, for decreasing fibre diameters. Measured mechanical and structural properties as a function of fibre diame-

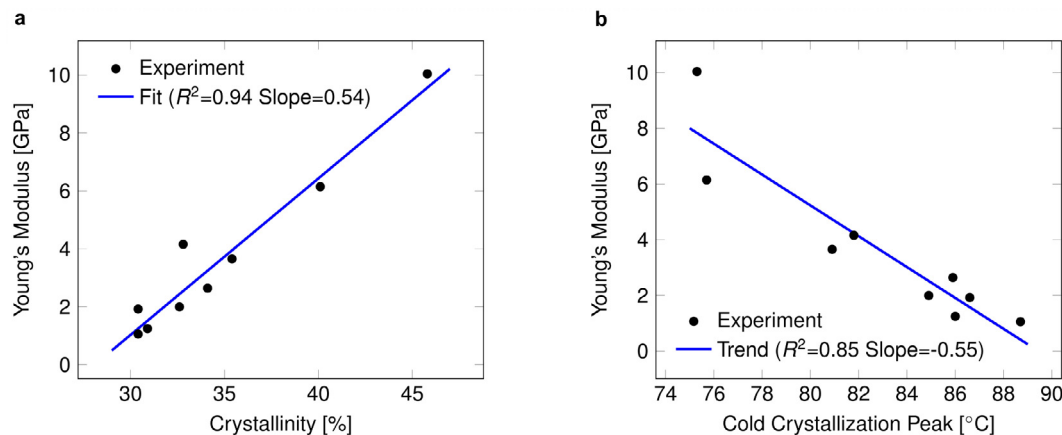


Fig. 10. Correlation of the Young's modulus with (a) the crystallinity and (b) the cold crystallization temperature.

ter show strong correlations. Using a power function (Fig. 6b) to capture the change of  $E$  with  $D$ ,  $E$  can be represented against crystallinity and cold crystallization peak temperature: Fig. 10a and 10b suggest a linear relationship between  $E$  and both structural parameters. Such a linear dependence could suggest a parallel arrangement of crystalline and amorphous phases, and thus support the presence of a core-shell structure of the fibres [48,62].

2D-WAXS patterns revealed that thinner fibres incorporate a higher fraction of oriented polymer chains. These experiments and analyses also confirmed that the orientation distribution of chains in the amorphous phase is narrower in thinner fibres and centred in the direction of the fibre axis. However, calculated orientation factors do not take into account the degree of (low) misorientation of the fibres within the network, leading to slightly biased values in the result similar for all membranes. A linear trend was observed between the orientation factor assessed by 2D-WAXS and cold crystallization peak temperature from DSC (Fig. 11). The fitted trend also suggests that for an isotropic amorphous phase ( $f_{H, \text{amorphous}} = 0$ ), corresponding CC peak temperature would be at 185 °C, which is very close to recorded melting temperatures ( $\sim 177$  °C). Correlating amorphous phase orientation measured by WAXS and cold crystallization peak temperature provides a promising approach for the investigation of the rearrangement of amorphous polymer chains during the cold crystallization process.

## 5. Conclusions

A comprehensive investigation of the elastic and inelastic mechanical, and morphological characteristics of PLLA fibres with diameters between 200 and 1400 nm prepared by needleless electrospinning was presented, whereby fibres of selected diameter sizes were analysed. For AFM-based three-point bending tests, an analytical relation between force and deflection was proposed based on a Timoshenko beam supported by torsional springs, which represents the effect of fibres being attached only at the bottom line of contact with their substrate. The model leads to consistently low errors below 10% for all tested diameters in the extraction of the Young's modulus, when compared to an inverse finite element model. A micromechanical testing system was used to extract inelastic material properties, i.e. yield stress and hardening modulus, while the values of Young's modulus agree well with those obtained from the AFM tests. The experiments reveal an increase of the Young's modulus by up to a factor of 10 for decreasing diameter below 800 nm. This phenomenon could be correlated with changes in structural properties, such as an increased crystallinity, stronger orientation of chains in the amorphous phase as well as a higher fraction of oriented polymer chains within thinner fibres. In particular, a linear trend between the Young's modulus and both crystallinity and cold crystallization temperature was observed. These results together with the improved method for analysis provide an important step towards understanding the relation between fibre geometry, morphology and mechanical properties, and towards developing fibres with tailored properties.

## Acknowledgements

The authors thank Felix Reifler and Anjani Maurya (Empa, Center for X-ray Analytics, Switzerland) for the helpful assistance with WAXS and SAXS experiments. The support of parts of this research, respectively, from the Swiss Competence Center for Materials Science and Technology (CCMX, Switzerland) and from the Swiss National Science Foundation (Project No. 155918) is gratefully acknowledged.

## Appendix A. Electrospinning solutions

**Table A.1**

Parameters of the electrospinning solutions used for the Nanospider.

[PLLA] [w/w]	DCM/DMF ratio [w/w]	[TEAB] [w/w of solvent]
3.5%	96/4	0.018%
6%	96/4	0.015%
7%	97/3	0.015%
8%	98/2	0.015%
9%	98/2	0.015%
10%	98/2	0.015%
12%	98/2	0.015%

## Appendix B. Ruland's streak method

The length and the overall orientation of longitudinal voids in polymer fibres can be evaluated by analysing the equatorial streaks of SAXS patterns [51,52]. When an azimuthal profile is fitted by a Lorentz function, the corresponding full width at half maximum  $B_{\text{obs}}$  is related to the length of the voids.  $B_{\text{obs}}$  can be determined at different scattering vectors  $q = 4\pi \sin(\theta)/\lambda$ , where  $2\theta$  is the scattering angle. Using Eq. (B.1), the void length  $L$  and the misorientation width  $B_{\Phi}$  can be determined. The latter describes the width of the orientation distribution of the voids and, since the voids are assumed to be aligned along the fibre axis, this is representative of the fibres misalignment [33,51] (Fig. B.1).

$$q^2 B_{\text{obs}}^2(q) = \frac{1}{L^2} + B_{\Phi}^2 q^2 \quad (\text{B.1})$$

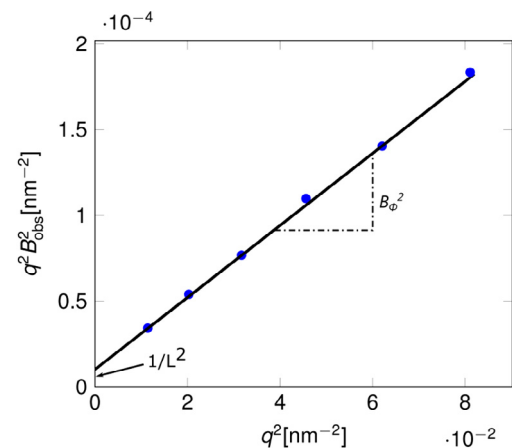


**Fig. B1.** Plot of Eq. (B.1) considering the equatorial streak of SAXS patterns for the membrane made from 10% PLLA uniaxially drawn to 40% of strain. It is used for the calculation of the voids misorientation  $B_{\Phi}$  and length  $L$ .  $B_{\text{obs}}(q)$  is the full width at half maximum of the azimuthal profile of the equatorial streaks at defined  $q$ -value.

## Appendix C. 2D-WAXS pattern analysis

2D-WAXS measurements (Fig. C.1a) were used to determine the respective orientation factors  $f_H$  (Eq. (7)) of the different material phases. Peak positions and FWHM have to be defined for each phase over the azimuthal axis (Fig. C.1b). In order to achieve this, peak fitting was first carried out on diffraction profiles (over  $2\theta$ -axis) at different azimuthal angle of the 2D-WAXS pattern with Gaussian functions (Fig. C.1c, d). Previous studies already performed peak fitting on diffraction profiles for PLLA samples. In most cases, the fittings comprise two broad peaks corresponding to the amorphous phase, one peak for the mesophase and, eventually, narrow crystalline peaks in case of highly crystalline samples

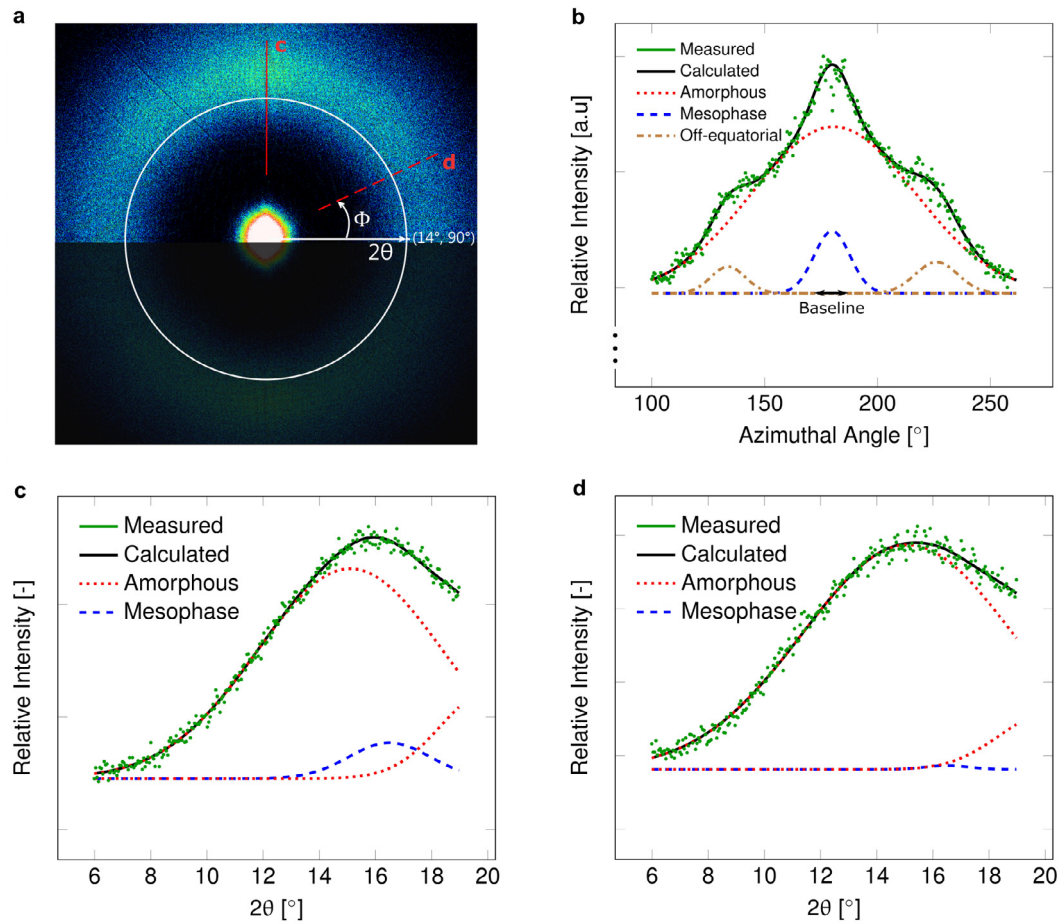


**Fig. C1.** Peak fitting of 2D-WAXS pattern. (a) 2D-WAXS pattern of membrane from 8% PLLA uniaxial stretched to 35% of strain. Radial  $2\theta$ -axis and azimuthal  $\Phi$ -axis are represented. Vertical fibre axis ( $\Phi = 180^\circ$ ) corresponding to the fibres axis in the reciprocal space is represented by the full line, azimuthal angle of  $115^\circ$  by the dashed line (b) Peak fitting of azimuthal profile of sample from 8% PLLA solution. Maximum intensity is located at equatorial position ( $180^\circ$ ). Two shoulders are visible at off-equatorial angles ( $\sim 135^\circ$  and  $\sim 225^\circ$ ). (c, d) Diffraction profiles at azimuthal angles (c)  $\Phi = 180^\circ$  and (d)  $115^\circ$ .

[38–40]. In the present study, mesophase peak position was determined according to the small peak visible on the diffraction profile of a membrane produced from 6% PLLA solution at  $2\theta = 16.5^\circ$  (Fig. 9f) corresponding to the (2 0 0/1 1 0) planes [38–40]. Amorphous broad peak positions were defined for each sample using the diffraction profile at azimuthal angle of  $115^\circ$  (Fig. C.1a (dashed line) and Fig. C.1d), where the mesophase is assumed to be lower than in the fibre direction (plain line in Fig. C.1a).

From the peak fitting over  $2\theta$ -axis the area under the Gaussian functions, characteristic for the respective phases, can be assessed for defined azimuthal angles (Fig. C.1c, d). The changes of respective areas over different azimuthal angles are used as criteria for the peak fitting of the multiple phases along the azimuthal axis (Fig. C.1b).

The off-equatorial peaks (Fig. C.1b) can be due to the slip or fragmentation of mesophase or crystalline structures during the electrospinning drawing process [63,64].

#### Appendix D. Error analysis

By a propagation of measurement uncertainties, one obtains the relative error  $\Delta E/E$  as

$$\frac{\Delta E}{E} = \frac{1}{E} \sqrt{\left(\frac{\partial E}{\partial F} \Delta F\right)^2 + \left(\frac{\partial E}{\partial L} \Delta L\right)^2 + \left(\frac{\partial E}{\partial D} \Delta D\right)^2 + \left(\frac{\partial E}{\partial \hat{w}} \Delta \hat{w}\right)^2}. \quad (\text{D.1})$$

For an Euler-Bernoulli beam (see Section 2.3.2), for example,  $E = (64FL^3)/(c\pi D^4 \hat{w})$  and (D.1) yields

$$\frac{\Delta E}{E} = \sqrt{\left(\frac{\Delta F}{F}\right)^2 + \left(3\frac{\Delta L}{L}\right)^2 + \left(4\frac{\Delta D}{D}\right)^2 + \left(\frac{\Delta \hat{w}}{\hat{w}}\right)^2}, \quad (\text{D.2})$$

irrespective of the value of the constant  $c$ . Eq. (D.1) was evaluated numerically with Matlab based on Eq. (1) for the AFM measurements, and on Eq. (2) for MMT. When comparing these errors with those predicted by (D.2), we found differences below 1%, and therefore, Eq. (D.2) was finally used to estimate the relative error for both AFM and MMT. The uncertainties for fibre length and diameter from SEM image analysis, estimated by repeated measurements ( $n = 5$ ), are  $\Delta L/L_{\text{AFM}} = 3\%$  and  $\Delta D/D_{\text{AFM,MMT}} = 5\%$ . Regarding AFM measurements  $\Delta F/F_{\text{AFM}} = 5\%$ ,  $\Delta \hat{w}/\hat{w}_{\text{AFM}} = 3\%$  was used based on previous studies [35]. Due to the high accuracy of the clamping set-up the error in fibre length for MMT measurement was set to  $\Delta L/L_{\text{MMT}} = 1\%$ . Based on the scatter in the force signal (0.5  $\mu\text{N}$  Fig. 8) and displacement resolution (5 nm) of the MMT device taken from the datasheet, the relative error was calculated for a mean force-displacement data point (2.5  $\mu\text{N}$ , 200 nm) occurring in the elastic regime (Fig. 8a) to  $\Delta F/F_{\text{MMT}} = 20\%$ ,  $\Delta \hat{w}/\hat{w}_{\text{MMT}} = 3\%$ . These values lead with Eq. (D.2) to a relative error of the Young's modulus of

$$\text{AFM: } \frac{\Delta E}{E} = 23\%, \quad \text{MMT: } \frac{\Delta E}{E} = 29\%.$$

The same relative error of 29% was used as an estimate for the error in yielding and hardening in MMT measurements.

**Appendix E. Analytic derivation of spring constant**

In order to connect the spring constant  $k$  of the rotational spring (Fig. 2) with the geometry and material properties of the fibre sticking to the substrate, a small rotation  $\varphi$  of the fibre cross-section is assumed to cause a linear displacement  $u$  (Fig. E.1). To calculate the corresponding strain  $\varepsilon$ ,  $u$  is divided by a characteristic length  $L_0$  so that  $\varepsilon = \varphi(y + D/2)/L_0$ . Representing  $L_0$  as a multiple  $\alpha$  of  $D$  ( $L_0 = \alpha D$ ), the resulting moment acting at  $z = 0$  can be calculated as

$$M = \int y\sigma dA = \int yE\varepsilon dA = \frac{E\varphi}{\alpha D} \left( \int y^2 dA + \frac{D}{2} \int y dA \right) = \frac{E\varphi}{\alpha D} \left( \int y^2 dA \right) = \frac{E\varphi I}{\alpha D}$$

Identifying the resulting moment with the moment caused by a rotational spring  $M = k\varphi$  gives

$$k = \frac{EI}{\alpha D}$$

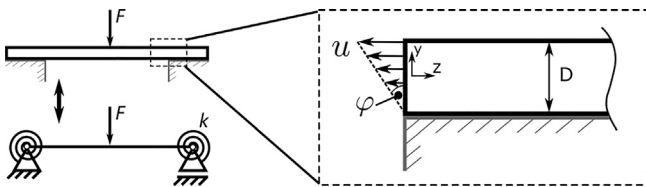


Fig. E1. Model of fibre lying on substrate to extract analytical description of moment.

**Appendix F. Symbols**

*F.1. Mechanical testing*

$A$	Fibre cross-sectional area
$c$	Constant specifying either DC or DS boundary conditions in analytical approach
$D$	Fibre diameter
$E$	Young's modulus
$E_{ana}$	Young's modulus calculated by analytical approach
$E_{iFEM}$	Young's modulus calculated by iFEM approach
$F$	Force
$G$	Shear modulus
$H$	Hardening
$I$	Second moment of inertia
$k$	Rotational spring constant
$L$	Free spanning fibre length
$L_0$	Characteristic length
$M$	Rotational Moment
$P$	Engineering stress
$P_Y$	Yield stress
$w$	Displacement
$w_A$	Displacement at point A (see Fig. 1b)
$w_B$	Displacement at point B (see Fig. 1b)
$w_{hook}$	Absolute displacement of hook in MMT measurement
$w_{off}$	Absolute displacement of hook when initially coming in contact with fibre
$\hat{w}$	Central displacement

$\hat{w}_{FE}$	Central displacement of beam calculated by FE simulation
$\alpha$	Characteristic length factor
$\beta$	Fibre deflection angle
$\varepsilon$	Engineering strain
$\eta$	Shear correction factor
$\kappa$	Boundary factor
$\nu$	Poisson's ratio
$\varphi$	Rotation angle

*F.2. WAXS and SAXS*

$2\theta$	Scattering angle
$A_{or}$	Area under of WAXS azimuthal profile but above the baseline
$A_b$	Area below the baseline of WAXS azimuthal profile
$B_\Phi$	Misorientation width
$B_{obs}$	Full width at half maximum
$f_H$	Orientation factor
$F_{or}$	Fraction of oriented polymer chains
$L$	Fibre voids length
$q$	Scattering vectors
$\Phi$	Azimuthal angle

*F.3. Differential scanning calorimetry*

$\Delta H_0$	Theoretical melting enthalpy of pure crystalline PLLA
$\Delta H_c$	Cold crystallization enthalpy
$\Delta H_m$	Melting enthalpy
$\bar{\chi}$	Crystallinity degree

**References**

- [1] F. Jian, N.I.U. Haitao, L.I.N. Tong, W. Xungai, Applications of electrospun nanofibers, Chinese Sci. Bull. 53 (2008) 2265–2286, <https://doi.org/10.1007/s11434-008-0319-0>.
- [2] H. Nie, M. Ho, C. Wang, C. Wang, Y. Fu, Biomaterials BMP-2 plasmid loaded PLGA/HAP composite scaffolds for treatment of bone defects in nude mice, Biomaterials 30 (2009) 892–901, <https://doi.org/10.1016/j.biomaterials.2008.10.029>.
- [3] J. Hrib, J. Sirc, R. Hobzova, Z. Hampejsova, Z. Bosakova, M. Munzarova, J. Michalek, Nanofibers for drug delivery - incorporation and release of model molecules, influence of molecular weight and polymer structure, Beilstein J. Nanotechnol. 6 (2015) 1939–1945, <https://doi.org/10.3762/bjnano.6.198>.
- [4] V. Leung, F. Ko, Biomedical applications of nanofibers, Polym. Adv. Technol. (2011) 350–365, <https://doi.org/10.1002/pat.1813>.
- [5] X. Zhao, X. Sun, L. Yildirimer, Q. Lang, Z.Y. (William) Lin, R. Zheng, Y. Zhang, W. Cui, N. Annabi, A. Khademhosseini, Cell infiltrative hydrogel fibrous scaffolds for accelerated wound healing, Acta Biomater. 49 (2017) 66–77, <https://doi.org/10.1016/j.actbio.2016.11.017>.
- [6] A.G. Guex, D. Hegemann, M.N. Giraud, H.T. Tevaearai, A.M. Popa, R.M. Rossi, G. Fortunato, Covalent immobilisation of VEGF on plasma-coated electrospun scaffolds for tissue engineering applications, Colloids Surfaces B Biointerfaces 123 (2014) 724–733, <https://doi.org/10.1016/j.colsurfb.2014.10.016>.
- [7] W. Xu, R. Shen, Y. Yan, J. Gao, Preparation and characterization of electrospun alginate/PLA nanofibers as tissue engineering material by emulsion electrospinning, J. Mech. Behav. Biomed. Mater. 65 (2017) 428–438, <https://doi.org/10.1016/j.jmbbm.2016.09.012>.
- [8] J. Voorneveld, A. Oosthuysen, T. Franz, P. Zilla, D. Bezuidenhout, Dual electrospinning with sacrificial fibers for engineered porosity and enhancement of tissue ingrowth, J. Biomed. Mater. Res. Part B Appl. Biomater. (2016) 1–14, <https://doi.org/10.1002/jbm.b.33695>.

- [9] L. Weidenbacher, A. Abrishamkar, M. Rottmar, A.G. Guex, K. Maniura-Weber, A. J. deMello, S.J. Ferguson, R.M. Rossi, G. Fortunato, Electrospinning of microfluidic encapsulated cells for the fabrication of cell-laden electrospun hybrid tissue constructs, *Acta Biomater.* 64 (2017) 137–147, <https://doi.org/10.1016/j.actbio.2017.10.012>.
- [10] T. Stylianopoulos, C.A. Bashur, A.S. Goldstein, S.A. Guelcher, V.H. Barocas, Computational predictions of the tensile properties of electrospun fiber meshes: effect of fiber diameter and fiber orientation, *J. Mech. Behav. Biomed. Mater.* 1 (2008) 326–335, <https://doi.org/10.1016/j.jmbmm.2008.01.003>.
- [11] B.R. Neugirg, S.R. Koebley, C. Schniepp, A. Fery, AFM-based mechanical characterization of single nano fibres (2016) 8414–8426, <http://doi.org/10.1039/c6nr00863a>.
- [12] B.R. Neugirg, M. Burgard, A. Greiner, A. Fery, Tensile versus AFM testing of electrospun PVA nanofibers: bridging the gap from Microscale to nanoscale, *J. Polym. Sci. Part B Polym. Phys.* (2016) 1–7, <https://doi.org/10.1002/polb.24225>.
- [13] E.P.S. Tan, C.T. Lim, Effects of annealing on the structural and mechanical properties of electrospun polymeric nanofibers, PLLA, *Nanotechnology* 17 (2006) 2649–2654, <https://doi.org/10.1088/0957-4484/17/10/034>.
- [14] D. Kluge, F. Abraham, S. Schmidt, H. Schmidt, A. Fery, M. Planck, Nanomechanical properties of supramolecular self-assembled whiskers determined by AFM force mapping, *Langmuir*. 26 (2010) 3020–3023, <https://doi.org/10.1021/la904780c>.
- [15] S.D. Hudson, V. Zhurov, V. Grbić, M. Grbić, J.L. Hutter, M. Grbić, Measurement of the elastic modulus of spider mite silk fibers using atomic force microscopy, *J. Appl. Phys.* 113 (2013), <https://doi.org/10.1063/1.4800865>.
- [16] A. Heidelberg, L.T. Ngo, B. Wu, M.A. Phillips, S. Sharma, T.I. Kamins, J.E. Sader, J. Boland, A generalized description of the elastic properties of nanowires, *Letters* (2006) 2–7, <https://doi.org/10.1021/nl060028u>.
- [17] S. Iwamoto, W. Kai, A. Isogai, T. Iwata, Elastic modulus of single cellulose microfibrils from tunicate measured by atomic force, *Microscopy* (2009) 2571–2576, <https://doi.org/10.1021/bm900520n>.
- [18] U. Stachewicz, R.J. Bailey, W. Wang, A.H. Barber, Size dependent mechanical properties of electrospun polymer fibers from a composite structure, *Polymer (Guildf)* 53 (2012) 5132–5137, <https://doi.org/10.1016/j.polymer.2012.08.064>.
- [19] S.R. Baker, S. Banerjee, K. Bonin, M. Guthold, Determining the mechanical properties of electrospun poly-ε-caprolactone (PCL) nanofibers using AFM and a novel fiber anchoring technique, *Mater. Sci. Eng. C*. 59 (2016) 203–212, <https://doi.org/10.1016/j.msec.2015.09.102>.
- [20] D. Papkov, Y. Zou, M.N. Andalib, A. Goponenko, S.Z.D. Cheng, Y.A. Dzenis, Simultaneously strong and tough ultra fine continuous nano fibers, (2013) 3324–3331, <http://doi.org/10.1021/nn400028p>.
- [21] E.P.S. Tan, S.Y. Ng, C.T. Lim, Tensile testing of a single ultrafine polymeric fiber, *Biomaterials* 26 (2004) 1453–1456, <https://doi.org/10.1016/j.biomaterials.2004.05.021>.
- [22] M.N. Silberstein, C. Pai, G.C. Rutledge, M.C. Boyce, Elastic–plastic behavior of non-woven fibrous mats, *J. Mech. Phys. Solids*. 60 (2012) 295–318, <https://doi.org/10.1016/j.jmps.2011.10.007>.
- [23] B. Janković, J. Pelipenko, M. Škarabot, I. Mušević, J. Kristl, The design trend in tissue-engineering scaffolds based on nanomechanical properties of individual electrospun nanofibers, *Int. J. Pharm.* 455 (2013) 338–347, <https://doi.org/10.1016/j.ijpharm.2013.06.083>.
- [24] M. Richard-Lacroix, C. Pellerin, Orientation and partial disentanglement in individual electrospun fibers: diameter dependence and correlation with mechanical properties, *Macromolecules* 48 (2015) 4511–4519, <https://doi.org/10.1021/acs.macromol.5b00994>.
- [25] A. Arinstein, M. Burman, O. Gendelman, E. Zussman, Effect of supramolecular structure on polymer nanofiber elasticity, *Nat. Nanotechnol.* 2 (2007) 59–62, <https://doi.org/10.1038/nnano.2006.172>.
- [26] C.T. Lim, E.P.S. Tan, S.Y. Ng, C.T. Lim, E.P.S. Tan, S.Y. Ng, Effects of crystalline morphology on the tensile properties of electrospun polymer nanofibers 141908 (2008) 2006–2009, <http://doi.org/10.1063/1.2857478>.
- [27] S.C. Wong, A. Bajji, S. Leng, Effect of fiber diameter on tensile properties of electrospun poly(ε-caprolactone), *Polymer (Guildf)* 49 (2008) 4713–4722, <https://doi.org/10.1016/j.polymer.2008.08.022>.
- [28] R. Inai, M. Kotaki, S. Ramakrishna, Structure and properties of electrospun PLLA single nanofibers, *Nanotechnology* 16 (2005) 208–213, <https://doi.org/10.1088/0957-4484/16/2/005>.
- [29] R. Jaeger, D. Jaeger, J. Schischka, Tensile testing of individual ultrathin electrospun poly(L-lactic acid) fibers, *J. Appl. Polym. Sci.* 114 (2009) 3774–3779, <https://doi.org/10.1002/app>.
- [30] X. Zhang, R. Nakagawa, K. Ho, K. Chan, M. Kotaki, Mechanical property enhancement of polylactide nano fibers through optimization of molecular weight, electrospinning conditions, and stereocomplexation, *Macromolecules* 45 (2012) 5494–5500, <https://doi.org/10.1021/ma300289z>.
- [31] G. Yazgan, R.I. Dmitriev, V. Tyagi, J. Jenkins, M. Rottmar, R.M. Rossi, C. Toncelli, D.B. Papkovsky, K. Maniura-weber, G. Fortunato, Steering surface topographies of electrospun fibers: understanding the mechanisms, (2017) 1–13, <http://doi.org/10.1038/s41598-017-00181-0>.
- [32] J. Liu, D.Y. Lin, B. Wei, D.C. Martin, Single electrospun PLLA and PCL polymer nanofibers: increased molecular orientation with decreased fiber diameter, *Polymer (Guildf)* 118 (2017) 143–149, <https://doi.org/10.1016/j.polymer.2017.04.070>.
- [33] T. Yano, Y. Higaki, D. Tao, D. Murakami, M. Kobayashi, N. Ohta, J.I. Koike, M. Horigome, H. Masunaga, H. Ogawa, Y. Ikemoto, T. Moriwaki, A. Takahara, Orientation of poly(vinyl alcohol) nanofiber and crystallites in non-woven electrospun nanofiber mats under uniaxial stretching, *Polym.* (United Kingdom) 53 (2012) 4702–4708, <https://doi.org/10.1016/j.polymer.2012.07.067>.
- [34] T. Yoshioka, R. Dersch, M. Tsuji, A.K. Schaper, Orientation analysis of individual electrospun PE nanofibers by transmission electron microscopy, *Polymer (Guildf)* 51 (2010) 2383–2389, <https://doi.org/10.1016/j.polymer.2010.03.031>.
- [35] F. Croisier, A.S. Duwez, C. Jérôme, A.F. Léonard, K.O. Van Der Werf, P.J. Dijkstra, M.L. Bennink, Mechanical testing of electrospun PCL fibers, *Acta Biomater.* 8 (2012) 218–224, <https://doi.org/10.1016/j.actbio.2011.08.015>.
- [36] J.S. Bergström, D. Hayman, An overview of mechanical properties and material modeling of polylactide (PLA) for medical applications, *Ann. Biomed. Eng.* 44 (2016) 330–340, <https://doi.org/10.1007/s10439-015-1455-8>.
- [37] Q. Wang, G. Fang, Y. Zhao, G. Wang, T. Cai, Computational and experimental investigation into mechanical performances of Poly-L-Lactide Acid (PLLA) coronary stents, *J. Mech. Behav. Biomed. Mater.* 65 (2017) 415–427, <https://doi.org/10.1016/j.jmbmm.2016.08.033>.
- [38] G. Stoclet, R. Seguela, J. Lefebvre, C. Rochas, New Insights on the Strain-Induced Mesophase of Poly(D, L-lactide): In Situ WAXS and DSC Study of the Thermo-Mechanical Stability, (2010) 7228–7237, <http://doi.org/10.1021/ma101430c>.
- [39] Q. Ma, M. Pyda, B. Mao, P. Cebe, Relationship between the rigid amorphous phase and mesophase in electrospun fibers, *Polymer (Guildf)* 54 (2013) 2544–2554, <https://doi.org/10.1016/j.polymer.2013.03.019>.
- [40] C. Zhou, H. Li, W. Zhang, J. Li, S. Huang, Direct investigations on strain-induced cold crystallization behavior and structure evolutions in amorphous poly(lactic acid) with SAXS and WAXS measurements, *Polymer (Guildf)* 90 (2016) 111–121, <https://doi.org/10.1016/j.polymer.2016.03.014>.
- [41] C. Zhou, H. Li, Y. Zhang, F. Xue, S. Huang, Deformation and structure evolution of glassy poly(lactic acid) below the glass transition, *CrystEngComm*. 17 (2015) 5651–5663, <https://doi.org/10.1039/C5CE00669D>.
- [42] M. Zündel, E. Mazza, A.E. Ehret, A 2.5D approach to the mechanics of electrospun fibre mats, *Soft Matter*. 13 (2017) 6407–6421, <https://doi.org/10.1039/C7SM01241A>.
- [43] C.A. Schneider, W.S. Rasband, K.W. Eliceiri, NIH Image to ImageJ: 25 years of image analysis, *Nat. Methods*. 9 (2012) 671–675, <https://doi.org/10.1038/nmeth.2089>.
- [44] H.-J. Butt, M. Jaschke, Calculation of thermal noise in atomic force microscopy, *Nanotechnology* 6 (1995) 1–7, <https://doi.org/10.1088/0957-4484/6/1/001>.
- [45] E. Onate, Structural Analysis with the Finite Element Method – Linear Statics: Volume 2: beams, plates and, shells (2013), <https://doi.org/10.1017/CBO9781107415324.004>.
- [46] C.M. Wang, Timoshenko beam-bending solutions in terms of euler-bernoulli solutions, *J. Eng. Mech.* 121 (1995) 763–765.
- [47] W. Weaver, J.M. Gere, Matrix Analysis of Framed Structures, 1990, <http://doi.org/10.1007/978-1-4684-7487-9>.
- [48] E.Y. Gómez-Pachón, F.M. Sánchez-Arévalo, F.J. Sabina, A.M. Rau, N. Batina, I.M. Ricardo, Characterisation and modelling of the elastic properties of poly(lactic acid) nanofiber scaffolds, *J. Mater. Sci.* 48 (2013) 8308–8319, <https://doi.org/10.1007/s10853-013-7644-7>.
- [49] D. Garlotta, A Literature Review of Poly(Lactic Acid), 9 (2002).
- [50] V. Hosseini, O. Evrova, S.P. Hoerstrup, V. Vogel, A simple modification method to obtain anisotropic and porous 3D microfibrillar scaffolds for surgical and biomedical applications, *Small* 14 (2018) 1–9, <https://doi.org/10.1002/smll.201702650>.
- [51] W. Ruland, Small-angle scattering studies on carbonized cellulose fibers\*, *J. Polym. Sci. Part C* 151 (1969) 143–151.
- [52] A.F. Thünemann, W. Ruland, Microvoids in polyacrylonitrile fibers: a small-angle X-ray scattering study, *Macromolecules* 33 (2000) 1848–1852, <https://doi.org/10.1021/ma991427x>.
- [53] X. Zong, K. Kim, D. Fang, S. Ran, B.S. Hsiao, B. Chu, Structure and process relationship of electrospun bioabsorbable nanofiber membranes, *Polymer (Guildf)* 43 (2002) 4403–4412, [https://doi.org/10.1016/S0032-3861\(02\)00275-6](https://doi.org/10.1016/S0032-3861(02)00275-6).
- [54] N.S. Murthy, R.G. Bray, S.T. Correale, R.A.F. Moore, Drawing and annealing of nylon-6 fibers - studies of crystal-growth, orientation of amorphous and crystalline domains and their influence on properties, *Polymer (Guildf)* 36 (1995) 3863–3873, [https://doi.org/10.1016/0032-3861\(95\)99780-x](https://doi.org/10.1016/0032-3861(95)99780-x).
- [55] P.H. Hermans, *Contributions to the Physics of Cellulose Fibers*, Elsevier, Amsterdam, 1946.
- [56] T. Kongkhleng, K. Tashiro, M. Kotaki, S. Chirachanchai, Electrospinning as a new technique to control the crystal morphology and molecular orientation of polyoxymethylene nanofibers, *J. Am. Chem. Soc.* 130 (2008) 15460–15466.
- [57] J.F. Mano, Y. Wang, J.C. Viana, Z. Denchev, M.J. Oliveira, Cold Crystallization of PLLA Studied by Simultaneous SAXS and WAXS, *Macromol. Mater. Eng.* (2004) 910–915, <https://doi.org/10.1002/mame.200400097>.
- [58] J. Zhang, K. Tashiro, H. Tsuji, A.J. Domb, Disorder-to-order phase transition and multiple melting behavior of poly(L-lactide) investigated by simultaneous measurements of WAXD and DSC, *Macromolecules* 41 (2008) 1352–1357, <https://doi.org/10.1021/ma0706071>.
- [59] M.A. Alamein, S. Stephens, Q. Liu, S. Skabo, P.H. Warnke, Mass production of nanofibrous extracellular matrix with controlled 3D morphology for large-

- scale soft tissue regeneration, *Tissue Eng. Part C Methods* 19 (2013) 458–472, <https://doi.org/10.1089/ten.TEC.2012.0417>.
- [60] E.A. Krogstad, K.A. Woodrow, Manufacturing scale-up of electrospun poly (vinyl alcohol) fibers containing tenofovir for vaginal drug delivery, *Int. J. Pharm.* 475 (2014) 282–291, <https://doi.org/10.1016/j.ijpharm.2014.08.039>.
- [61] Y. Chen, B.L. Dorgan, D.N. Mcilroy, D.E. Aston, Y. Chen, B.L. Dorgan, D.N. Mcilroy, On the importance of boundary conditions on nanomechanical bending behavior and elastic modulus determination of silver nanowires, *J. Appl. Phys.* 100 (2009), <https://doi.org/10.1063/1.2382265>.
- [62] S.J. Eichhorn, R.J. Young, The Young's modulus of a microcrystalline cellulose, *Cellulose* 8 (2001) 197–207, <https://doi.org/10.1023/A:1013181804540>.
- [63] X. Zhang, K. Schneider, G. Liu, J. Chen, K. Brüning, D. Wang, M. Stamm, Deformation-mediated superstructures and cavitation of poly(L-lactide): in-situ small-angle X-ray scattering study, *Polymer (Guildf)* 53 (2012) 648–656, <https://doi.org/10.1016/j.polymer.2011.12.002>.
- [64] G. Stoclet, R. Seguela, C. Vanmansart, C. Rochas, J. Lefebvre, WAXS study of the structural reorganization of semi-crystalline polylactide under tensile drawing, *Polymer* 53 (2012) 519–528, <http://doi.org/10.1016/j.polymer.2011.11.063>.